Hematocrit influences rare cell trajectories and capture rate in periodic obstacle arrays[1]

Martin Bušík[2], Iveta Jančigová[2,3], Renáta Tóthová[2], Ivan Cimrák[4]

Cell-in-fluid Research Group, http://cell-in-fluid.fri.uniza.sk
Faculty of Management Science and Informatics, University of Žilina
Univerzitná 8215/1, 010 26 Žilina, Slovakia

Abstract

Microfluidic devices containing periodic obstacle arrays are frequently used for capture of rare cells such as circulating tumour cells (CTC). Detailed computational analysis can give valuable insights into understanding of fluidic processes inside such devices.

Using our previously developed Object-in-fluid framework, we have investigated characteristics of single CTC inside a suspension of red blood cells. Further, we have developed new model for evaluation of cell capture probability that includes the surface area of the cell-obstacle contact. We have analyzed individual trajectories of CTC and their distribution between the obstacles during the transport through the device.

In our study, we focus on different levels of hematocrit. Our hypothesis is that higher cell density influences the CTC trajectories, their distributions between the obstacles, as well as the probability of cell capture computed by the newly developed model. We present the computational simulations confirming this hypothesis.

Keywords: periodic obstacle array, simulation study, capture rate
PACS: 83.10.Bb, 83.10.Rs, 87.17.Aa

[1]This work was supported by the Slovak Research and Development Agency under the contract No. APVV-0441-11.

[2]The work of Iveta Jančigová, Renáta Tóthová and Martin Bušík was supported by the FVG 2014 grant of Faculty of Management Science and Informatics, University of Žilina.

[3]e-mail of corresponding author: iveta.jancigova@fri.uniza.sk

[4]The work of Ivan Cimrák was supported by the Marie-Curie grant No. PCIG10-GA-2011-303580.

1. Introduction

Microfluidic devices with periodic obstacle arrays such as those described in [1] or [2] are very useful for particle or cell separation or capture. During the optimization of their design, such as in [3], often simplifying assumptions are made: model with only tracers instead of actual cells or one-way interaction of fluid and the cells immersed in it. In this simulation study, we present evidence that when optimizing devices for capture of rare cell from blood suspension, it is necessary to include the red blood cells (RBCs) in the model, because their influence on capture rate is not negligible.

The paper is organized as follows. We start with concepts leading to our measure of capture rate. Then we describe the simulation experiments that we have performed. We investigate the overall behavior of RBCs and the rare cell. And finally, we present results that show dependence of capture rate on the hematocrit.

2. Capture model formulation

The study published in [4] analyzes impact of shear stress near the wall on the adhesion of live cells. The cells in this study are LNCaP cells, human prostate cancer cells. The functionalization of walls is done with J591, a monoclonal antibody that targets the prostate specific membrane antigen (PSMA) expressed on LNCaP cells. The experiments were performed in Hele-Shaw chamber that is specifically designed to cover broad range of shear stresses in a single experiment. For specific details on materials, microdevice fabrication, functionalization of the walls, and cell maintenance, we refer to [4].

The goal of the study was to determine the dependence of capture rate on the shear stress. Several observation windows have been defined along the Hele-Shaw chamber with different shear stress in each window. Cells were injected into the device and some have been captured in the observation windows. After the experiment, the captured cells have been counted and the dependence show in Figure 1 was determined.

2.1. Existing cell capture models

Modelling of individual bonds formation between cells and functionalized surfaces requires inclusion of parameters whose physical values are largely

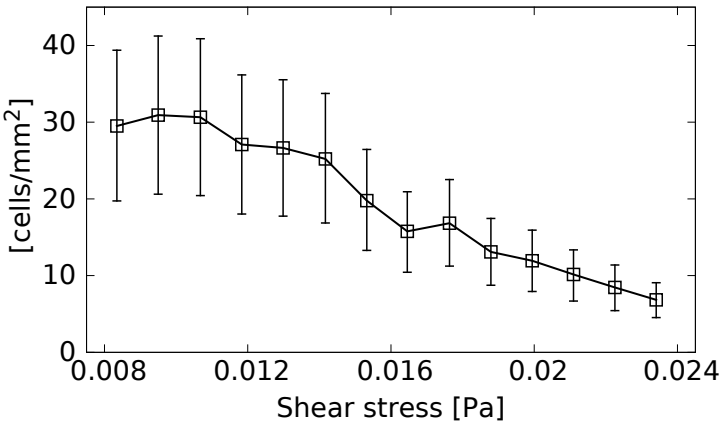

Figure 1: Experimental data defining the dependence of capture rate on the shear stress, redrawn from [4]. Density of captured cells is on y-axis.

unavailable for rare cell capture applications. To circumvent this, reduced models can be used. In [5], the authors present relatively simple exponential model for cell capture in linear shear flow. This model predicts the probability of adhesion in a simple channel as

$$P_a \simeq m_r m_l K_a^0 A_c \ \exp\left[-\frac{\lambda f}{k_B T}\right], \tag{1}$$

where m_r, m_l is the surface density of receptors and ligands; K_a^0 is the association constant at zero load of the ligand-receptor pair; A_c is the area of interaction between the cell and functionalized surface; f is the force per unit ligand–receptor pair; λ is a characteristic length of the ligand-receptor bond; $k_B T$ is the Boltzman thermal energy.

The quantity f is hard to determine and is often approximated using dislodging hydrodynamic force of the cell moving under given shear stress. Assuming uniform distribution of dislodging force over all active bond-ligand couples, the force f per unit ligand-receptor bond can be expressed as the ratio between the total dislodging force F_{dis} and the area of interaction A_c multiplied by the surface density of the receptors m_r, that is

$$f = \frac{F_{dis}}{m_r A_c}. \tag{2}$$

Complementing (1) with (2), the capture rate can be expressed as

$$P_a \simeq m_r m_l K_a^0 A_c \ \exp\left[-\frac{\lambda}{k_B T}\frac{F_{dis}}{m_r A_c}\right]. \tag{3}$$

In linear shear flow the dislodging force F_{dis} can be linearized near the wall and thus F_{dis} is taken proportional to the shear stress τ. In [3], the authors suggested to group multiple parameters into two lumped parameters A and B resulting in the following capture model

$$P_a \simeq A \ \exp\left[-B\tau\right]. \tag{4}$$

The parameters A and B must be calibrated using experimental data. Assuming the model (4) will be used for the same cells and the same surface chemistry as in [4], the parameter B can be calibrated from Figure 1 and the authors determined $B = 85.5Pa^{-1}$ to be the best exponential fit to experimental data.

Resulting parameter A was calibrated by simulating the microfluidic device with periodically repeating blocks of cylindrical obstacles. In [6] the authors perform a microfluidic experiment with the same cells and surface chemistry as in [4] to measure efficiency of cell capture in a specific device. They claim 70% capture efficiency of such device. This result has been used in [3] to calibrate A. They set up a computational model for the very same device as in [6] and they simulated the cell flow with capture modeled by (4) with $B = 85.5Pa^{-1}$ and with various values of A. For each value of A they obtained a capture efficiency and this way they determined value $A = 3.44 \times 10^{-2}s^{-1}$ to give 70% efficiency.

The capture model (4) has been used for optimization of microfluidic devices with periodically repeating cylindrical obstacles. The authors in [3] use CFD-particle advection simulation to track cells through a range of obstacle array geometries.

2.2. New model for cell capture

The model (4) was derived by simplifying the more complex model (3). Parameters A and B grouped several other parameters. The only variable left was τ. Assuming the same cell and surface chemistry, the parameters $m_r, m_l, K_a^0, \lambda, k_B$ and T are constant and they may be safely included under lumped parameters A and B. However, the area of interaction between cell and surface A_c varies with different τ. In fact, cells may deform under the

shear stress and the cells may have ellipsoidal shapes with different aspect ratios for different shear stresses. In [5], the authors analyze ellipsoidal shaped particles and they show that A_c changes under different aspect ratios. The contact area also varies with parameters of obstacles, e.g. increases with increasing column radius.

Another reason to keep A_c variable in the capture model is that such model would be usable also in dense suspensions, where cell contact area may vary under the cell-cell collisions.

These considerations lead us to propose the following model for cell capture:

$$P_a \simeq aA_c \ \exp\left[-b\frac{\tau}{A_c}\right]. \tag{5}$$

Similarly as in [3], we group several parameters, however we keep A_c variable. To calibrate our new model parameters a and b we can follow the previously described steps. For experiment in [4] we can compute the contact area $A_c^* = 2.47\mu m^2$ for cells used in that experiment. This computation is performed in the Appendix.

To be consistent with model (4), we put $A = aA_c^*$ and $B = b/A_c^*$ resulting in the following parameters for our new capture model

$$a = A/A_c^* = \frac{0.0344}{2.47} = 13.927 \times 10^{-3} s^{-1}\mu m^{-2} \tag{6}$$

$$b = B \cdot A_c^* = 85.5 \cdot 2.47 = 211.185 Pa^{-1}\mu m^2 \tag{7}$$

3. Computational model for cell flow

In our simulation study, we use the fully 3D model described in [7] that we have implemented as part of an open source scientific package ESPResSo [8, 9]. We use lattice-Boltzmann method [10] for fluid calculations and a spring network model for elastic behavior of the immersed blood cell. In this model we have local information about each point of the triangulation mesh - from its position and velocity to the magnitudes of acting elastic forces that conserve the volume, local and global area and shape of the cell.

The cell-fluid interaction is two-way, which means that not only the fluid advects the cells, but also the cells act on the fluid, which is important especially in dense suspension.

4. Description of simulation experiments

Our goal was to study a periodic obstacle array in a microfluidic device. However, simulation of such array with resolution that would allow us to see the effects of cell-cell interactions would be extremely computationally intensive. Therefore, we have simulated one block of this array, as depicted in Figures 2 and 3 and assumed periodicity in x and y directions. The dimensions of the simulated chamber were $100\mu m \times 50\mu m \times 30\mu m$.

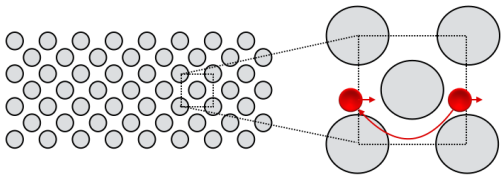

Figure 2: Periodic obstacle array

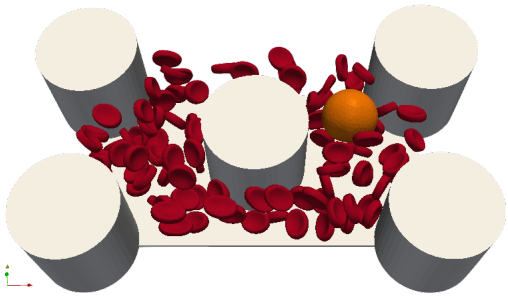

Figure 3: Chamber used in our simulations

While we do not perform rigorous optimisation of device geometry, we investigate four different sizes of cylindrical obstacles, to demonstrate the hematocrit effects under various conditions. The considered radii of micro-posts were 7, 9, 11 and $13\mu m$. Increase in radius leads to more frequent cell-obstacle collisions, however, the shear flow is increased too, which lowers the capture probability and our simulations show details about such inter-play.

We have simulated the pass of one rare cell (e.g. circulating tumour cell) in a suspension of red blood cells with different hematocrit through the chamber. For each column radius, the number of RBCs was 10, 50 and 100 and they were seeded at random positions.

4.1. Fixed flow rate

We have kept the volumetric flow rate constant. As described in [1], we consider the maximal shear rate $\tau_{max} = 0.04Pa$ at the obstacle boundaries. We design our experiments in such a way that this shear rate is achieved with columns with $r = 7\mu m$, compute the corresponding volumetric flow rate and then keep this flow rate fixed across the simulations with different radii.

In order to achieve this, we have simulated a channel with obstacles with diameter $r = 11\mu m$. We varied the force density in the simulation and observed the shear rate at several points around the central column and determined the force density f_{11} and corresponding volumetric flow rate Q_{11}, which give the maximal shear rate $\tau_{max} = 0.04Pa$. The volumetric flow rate Q is calculated as an integral of velocity profile at the $x = 0$ plane. In the following simulations, it is held constant at the value Q_{11}, i.e. proper force densities f_7, f_9, f_{13} are determined that result in flow rates $Q_7 = Q_9 = Q_{11} = Q_{13}$ in arrays with different obstacles.

4.2. CTC seeding

For each combination of column radius (4 values) and hematocrit (3 values) we have used 10 different seedings of CTC on the left-hand side of the simulated chamber ($x = 0$). These we regularly spaced in the opening between the two columns. We have repeated each of these simulations 10 times with different (random) RBC seedings. This resulted in the total number of 1,200 performed simulations. The CTCs were modeled as spheres with radius $r_{CTC} = 8.75$. (RBCs have a typical biconcave shape with diameter $r_{RBC} = 3.91$.)

5. Results

5.1. Observed characteristics

The distribution of red blood cells at the right-hand side of the chamber ($x = 100\mu m$) has a characteristic two peak shape (Figures 4, 5), which is due to fluid streamlines that, in general, take the cells away from the central point between columns.

As expected, the CTC trajectories behave differently in simulations with small number of RBCs and large number of RBCs, Figures 6, 7. While in simulations with 10 RBCs, where they basically do not come into contact with other cells, they fall into the same pattern, in simulations with 100 RBCs this pattern is quite often disturbed due to cell-cell contacts.

5.2. Estimate of number of passes through the device

In our investigation, we assume the obstacle density $80mm^{-2}$. This corresponds to the microfluidic device described in [1], which had 78,000 microposts covering the area of $970mm^2$. It also means about 9 passes of the

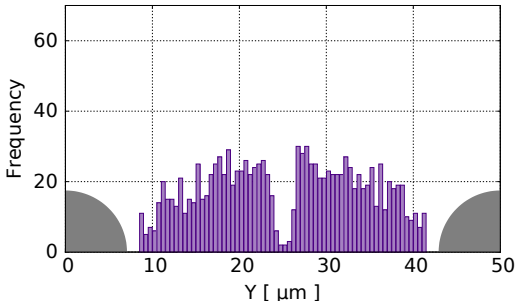

Figure 4: Distribution of y-coordinates of RBCs between two columns, $r = 7$

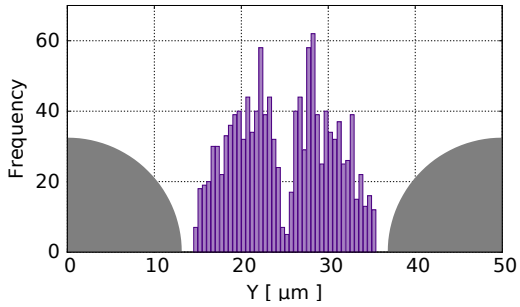

Figure 5: Distribution of y-coordinates of RBCs between two columns, $r = 13$

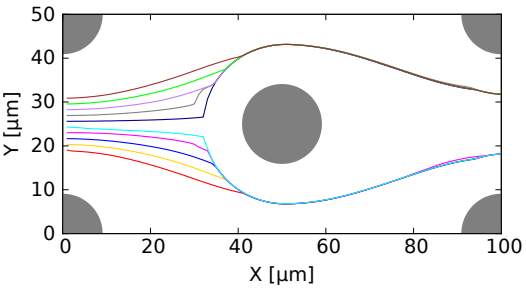

Figure 6: Typical CTC trajectories in simulations with 10 RBCs. Each line corresponds to a CTC center in different CTC seeding.

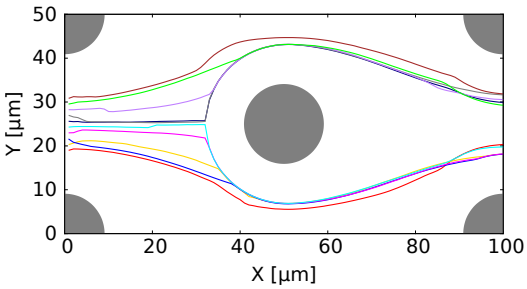

Figure 7: Typical CTC trajectories in simulations with 100 RBCs. Each line corresponds to a CTC center in different CTC seeding.

periodic chamber per mm. The area $970mm^2$ may be approximately represented by a rectangle $44mm \times 22mm$, which then gives $44 \cdot 9 \approx 400$ passes of a periodic block for a rare cell flowing through a microfluidic device. We denote this number by N_{pass} and use it in the following calculation of capture rate.

5.3. Typical distribution of CTCs between obstacles

We would like to determine the typical distribution of the $y-$coordinate of CTC at the right end of the simulation chamber and use it in the calculation of the capture rate over N_{pass} passes of the chamber without the need to actually simulate such a long process. Clearly, the CTC positions will not be distributed uniformly between the two cylindrical obstacles. To determine the typical distribution of $y-$coordinate of CTC, we start with

uniform distribution.

With fixed hematocrit we use the simulations with 10 regularly spaced initial $y-$coordinates of the CTC. The x-coordinate is zero for all of them. We record the final y-coordinate at the outflow in each of the 10 simulations with different random seeding of red blood cells. This way we obtain 100 final CTC positions.

We denote vector of initial positions $[p_1, \ldots, p_{10}]$, vector of final positions $[q_1, \ldots, q_{100}]$ and the corresponding vector of weights after i iterations $\mathbf{w} = [w_1^i, \ldots, w_{100}^i]$, which is set to $[1, \ldots, 1]$ at the beginning. After each hypothetical CTC pass of the simulated chamber, we redistribute the vector of weights using simulation results. For each final position q_j, we look for the closest initial positions p_{upper} and p_{lower}, such that $p_{upper} > q_j > p_{lower}$. We compute the weights $\alpha = (p_{upper} - q_j)/(p_{upper} - p_{lower})$ and $(1 - \alpha)$. We then add the weight 0.1α to each of the 10 CTC trajectories starting form p_{lower} and $0.1(1 - \alpha)$ to each of the 10 CTC trajectories starting from p_{upper}. The new weights $\mathbf{w}_{new}$ are then obtained as $\mathbf{w}_{old}$ multiplied by the obtained weights of CTC trajectories in this iteration.

The final weights represent the distribution of CTC positions at the end of the simulation chamber (in x direction). We have repeated this process N_{pass} times for the four column diameters and obtained the distributions depicted in Figures 8-11. Note, all of them show two peaks due to the symmetric nature of the problem.

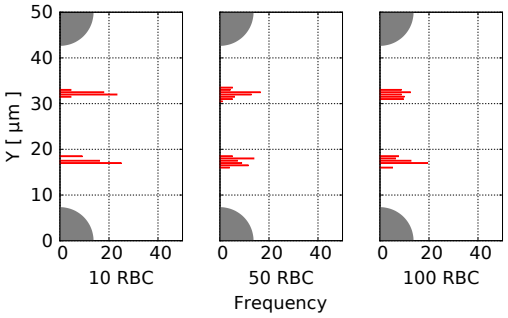

Figure 8: Histogram of typical CTC positions between two obstacles with $r = 7$, $N_{pass} = 400$.

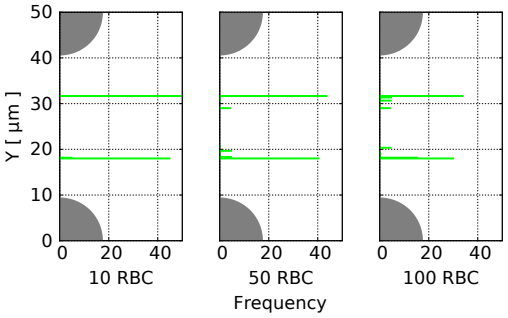

Figure 9: Histogram of typical CTC positions between two obstacles with $r = 9$, $N_{pass} = 400$.

As we can see, with increasing number of RBCs in the simulation, the CTC distributions are "wider". This means that the red blood cells have

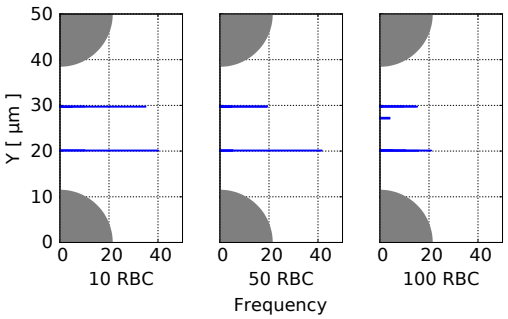

Figure 10: Histogram of typical CTC positions between two obstacles with $r = 11$, $N_{pass} = 400$.

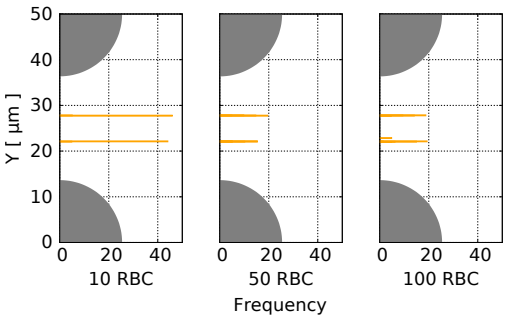

Figure 11: Histogram of typical CTC positions between two obstacles with $r = 13$, $N_{pass} = 400$.

impact on the CTC trajectory and cannot be neglected in the optimisation of periodic obstacle arrays.

5.4. Variance of final positions

To quantify the effect of RBCs on the CTC distributions, we have computed the means and variances for all 12 types of simulations (4 column radii, 3 values of hematocrit). These calculations cannot be computed directly from the resulting y-coordinates, since the whole simulation is symmetric and the two-peak distribution has mean significantly different from the two most often occurring values. Therefore, we have "folded" the final distribution in half (taking $50 - y$ instead of y for the upper half of data), and computed the mean and variance from the combined data. While the means remain consistent across the different values of hematocrit, the variance increases significantly, see Table 1.

5.5. Capture rates

We have also calculated the capture rate over the N_{pass} passes of the periodic chamber as

$$P = \sum_{i=1}^{N_{pass}} \sum_{j=1}^{100} w_j^i P_j \tag{8}$$

where P_j is calculated using (5). Results are summarized in Table 1 and we can see, that with larger obstacle radii, the capture rate is decreasing with increasing number of RBCs. Note, the P is not a probability that the cell will be captured in the corresponding pass through the device, but rather a characteristic measure that can be used to compare different device designs.

Table 1: Characteristics of the CTC distributions and corresponding capture rates

	r = 7			r = 9		
	P	**mean**	**var**	**P**	**mean**	**var**
10 cells	1.4320	17.5994	0.2335	13.7494	18.2061	0.0026
50 cells	1.7789	17.5164	0.5456	12.5408	18.4217	0.4304
100 cells	2.0142	17.6455	0.4751	12.1251	18.5042	0.5495

	r = 11			r = 13		
	P	**mean**	**var**	**P**	**mean**	**var**
10 cells	38.1193	20.2003	0.0026	76.4824	22.1843	0.0028
50 cells	36.5945	20.1864	0.0025	77.3349	22.1625	0.0030
100 cells	34.9334	20.3855	0.4990	73.3848	22.1779	0.0277

6. Discussion and conclusions

Our simulations show that higher hematocrit influences the trajectories of CTC. In Figure 7, see trajectory deviations caused by RBCs being in the way of moving CTCs. The statistics of deviations are clearly visible in Figures 8–11. For the whole range of obstacle radii we see a consistent increase of CTC deviations when increasing the hematocrit. The values of variance from the mean position of CTC between the obstacles are presented in Table 1. Here we see that for obstacle radius $7\mu m$, there is only a moderate increase in variance ($\times 2$), while for radii 9, 11 and $13\mu m$, the variance may increase by factor from 10 to 200.

Newly developed model for capture rate also confirmed the studied hypothesis. In Table 1 we see that increased hematocrit influences the capture rate (column P). Detailed analysis of the results however reveals interesting observation: For obstacle radius $7\mu m$, the capture rate increases with increased RBC count from 50 to 100 while for other radii, capture rate decreases. One possible explanation is that there is more physical space available in the microchannel with $r = 7\mu m$. At this radius, RBCs push the CTC towards the obstacle which results in increased capture rate but they still do have enough physical space not to get between the CTC and the obstacle.

Different behaviour can be seen at obstacle radii 9, 11 and 13 μm. Here, although RBCs push the CTC towards the obstacle, they have less space and they get between the CTC and the obstacle. This contributes to decrease of overall capture rate with increasing number of RBC from 50 to 100.

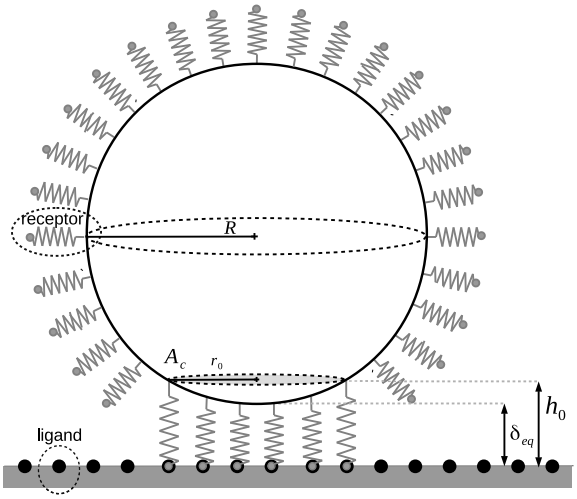

Figure 12: Spherical cell adhered to surface, redrawn from [5].

To summarize, we demonstrated that hematocrit influences the CTC behaviour in periodic obstacle arrays. This means that for correct analysis of periodic obstacle arrays, full three dimensional simulations involving cell-cell interactions are necessary. In addition to that, our new model shows that increasing the obstacle radius increases the capture rate.

Appendix

The cells used in experiments in [4] are considered spherical with radius $R = 17.5/2 = 8.75\mu m$. The contact area A_c is defined as projection of that part of the cell that is in the distance at most h_0 from the surface. Moreover, the distance of the cell from the surface during the adhesion contact is at least δ_{eq}, see Figure 12. Physiologically relevant value for $\delta_{eq} = 5 \cdot 10^{-9}m$ is taken from [5]. h_0 is the length of the combined receptor-ligand couple. However, there are different values reported in different sources. In the pioneering work [12], the author reports the ratio of bond length to cell radius in the range from 0.002 to 0.01. Korn [13] reports $h_0 = 5 \cdot 10^{-8}m$. Fedosov [14] reports $h_0 = 3.5 \cdot 10^{-7}m$. The following computation uses the value $h_0 = 5 \cdot 10^{-8}m$. Using the radius $R = 8.75 \cdot 10^{-6}m$ we can compute $A_c^* = \pi r_0^2$, where r_0 satisfies

$$r_0^2 + (R - (h_0 - \delta_{eq}))^2 \quad = \quad R^2 \tag{9}$$

$$
\begin{aligned}
r_0^2 &= 2R(h_0 - \delta_{eq}) - (h_0 - \delta_{eq})^2 \\
r_0^2 &= 17.5(0.05 - 0.005) - (0.05 - 0.005)^2 \\
r_0^2 &\doteq 0.785 \mu m^2
\end{aligned}
$$

which results in $A_c^* \doteq 2.47 \mu m^2$.

References

[1] S. Nagrath, et al., Isolation of rare circulating tumour cells in cancer patients by microchip technology, Nature 450 (2007) 1235–1239, ISSN 0028-0836.

[2] L. R. Huang, E. C. Cox, R. H. Austin, J. C. Sturm, Continuous Particle Separation Through Deterministic Lateral Displacement, Science 304 (5673) (2004) 987–990.

[3] J. Smith, T. Lannin, Y. Syed, S. Santana, B. Kirby, Parametric control of collision rates and capture rates in geometrically enhanced differential immunocapture (GEDI) microfluidic devices for rare cell capture, Biomedical Microdevices 16 (1) (2014) 143–151.

[4] S. Santana, H. Liu, N. Bander, J. Gleghorn, B. Kirby, Immunocapture of prostate cancer cells by use of anti-PSMA antibodies in microdevices, Biomedical Microdevices 14 (2) (2012) 401–407.

[5] P. Decuzzi, M. Ferrari, The adhesive strength of non-spherical particles mediated by specific interactions, Biomaterials 27 (30) (2006) 5307 – 5314.

[6] J. P. Gleghorn, et al., Capture of circulating tumor cells from whole blood of prostate cancer patients using geometrically enhanced differential immunocapture (GEDI) and a prostate-specific antibody, Lab Chip 10 (2010) 27–29.

[7] I. Cimrák, M. Gusenbauer, T. Schrefl, Modelling and simulation of processes in microfluidic devices for biomedical applications, Computers and Mathematics with Applications 64 (3) (2012) 278 – 288.

[8] I. Cimrák, M. Gusenbauer, I. Jančigová, An ESPResSo implementation of elastic objects immersed in a fluid, Computer Physics Communications 185 (3) (2014) 900 – 907, ISSN 0010-4655.

[9] A. Arnold, et al., ESPResSo 3.1 - Molecular Dynamics Software for Coarse–Grained Models, in: M. Griebel, M. Schweitzer (Eds.), Meshfree Methods for Partial Differential Equations VI, Lecture Notes in Computational Science and Engineering, vol. 89, 1–23, 2013.

[10] A. J. C. Ladd, Numerical simulations of particulate suspensions via a discretized Boltzmann equation. Part 2. Numerical results, Journal of Fluid Mechanics 271 (1994) 311–339, ISSN 1469-7645.

[11] R. Tóthová, I. Jančigová, M. Bušík, Calibration of elastic coefficients for spring-network model of red blood cell, in: Information and Digial Technologies (IDT) 2015, International Conference, IEEE, 376–380, 2015.

[12] D. A. Hammer, S. M. Apte, Simulation of cell roling and adhesion on surfaces in shear flow: general results and analysis of selectin-mediated neutrophil adhesion, Biophysical Journal 63 (1992) 35–57.

[13] C. B. Korn, U. S. Schwarz, Dynamic states of cells adhering in shear flow: From slipping to rolling, Phys. Rev. E 77 (2008) 041904.

[14] D. A. Fedosov, B. Caswell, G. E. Karniadakis, Wall Shear Stress-Based Model for Adhesive Dynamics of Red Blood Cells in Malaria, Biophysical Journal 100 (2011) 2084–2093.